Acta Materialia 246 (2023) 118728

Contents lists available at ScienceDirect

Acta Materialia

journal homepage: www.elsevier.com/locate/actamat

CALPHAD-aided design for superior thermal stability and mechanical behavior in a TiZrHfNb refractory high-entropy alloy

Tianxin Li [a], Shudao Wang [a], Wenxue Fan [a], Yiping Lu [a,b,c,*], Tongmin Wang [a,b,c], Tingju Li [a], Peter K. Liaw [d]

[a] Key Laboratory of Solidification Control and Digital Preparation Technology (Liaoning Province), School of Materials Science and Engineering, Dalian University of Technology, Dalian 116024, China
[b] Engineering Research Center of High entropy Alloy Materials (Liaoning Province), School of Materials Science and Engineering, Dalian University of Technology, Dalian 116024, China
[c] New Materials Innovation Center, Ningbo Institute of Dalian University of Technology, Ningbo 315000, China
[d] Department of Materials Science and Engineering, The University of Tennessee, Knoxville, TN 37996, United States

ARTICLE INFO

Keywords:
CALPHAD
High-entropy alloys
Mechanical property
Strengthening mechanism

ABSTRACT

TiZrHfNbTa refractory high-entropy alloys (RHEAs) are now at the research frontier of advanced metallic materials due to their exceptional mechanical performance, particularly at high temperatures. However, the TiZrHfNbTa RHEAs exhibit poor phase stability at intermediate temperatures (600 – 1,000 °C). The present study aimed to tailor their phase stability and mechanical properties *via* the calculation of phase diagrams (CALPHAD) approach. We found that Ta and Hf were detrimental to the phase stability of the TiZrHfNbTa RHEAs. Accordingly, a Ta-free and Hf-depleted $Ti_{30}Zr_{30}Hf_{16}Nb_{24}$ RHEA with outstanding phase stability was designed, which could remain a single-phase body-centered cubic (BCC) structure after annealing at 600 °C for 200 h. Furthermore, numerous (Ti, Zr)-rich nano-precipitates were dispersedly formed in the cold-rolled plus recrystallization-annealed (CR+A) $Ti_{30}Zr_{30}Hf_{16}Nb_{24}$ RHEA. The nano-precipitates controlled by the spinodal decomposition mechanism had an identical BCC lattice. The lattice fringes with $(1\bar{1}0)$ Miller indices bent from the matrix phase to the nano-precipitates, causing a strong local strain field near the phase boundaries. The CR+A alloy possessed a yield strength of ~ 800 MPa and tensile fracture elongation of ~ 34.0%, showing a superior strength-ductility combination. The strain measurement by a digital image correlation indicated that the CR+A alloy exhibited a more substantial plastic stability than the as-cast alloy. Detailed observations of deformation microstructures through a transmission electron microscope and electron back-scattered diffraction revealed the origin of strength and ductility. Dislocation cross-slip and kink bands tended to form in the CR+A alloy during deformation and were capable of accommodating dislocation slip against stress concentration. Labusch's model uncovered that solid-solution strengthening contributed the most to yield strength. The present study provides a paradigm for the superior thermostability and controllable nanophase-precipitation behavior in RHEAs.

1. Introduction

In the last decade, refractory high-entropy alloys (RHEAs) have attracted particular attention due to their exceptional high-temperature mechanical performance, making them potential materials to replace conventional superalloys [1–3]. Although numerous RHEAs with high strengths have been developed so far, the mechanical properties of most of them were studied using compression tests [4]. Tensile properties were reported for only a small subclass of RHEAs, the TiZrHfNbTa group [5], and its subsystems [6]. In other words, the TiZrHfNbTa group is one of the most widely studied and promising RHEAs.

The TiZrHfNbTa RHEAs in the as-cast state [5], as well as after annealing at a temperature above ~ 1000 °C [7], could remain stable as a body-centered cubic (BCC) solid solution owing to a large contribution of the configurational entropy in the Gibbs free energy expression. However, previous research has established that the TiZrHfNbTa RHEAs exhibit poor phase stability at intermediate temperatures (600 – 1000 °C) [8–10]. Phase transformation into a thermodynamically more

* Corresponding author.
E-mail addresses: luyiping@dlut.edu.cn, 82713860@qq.com (Y. Lu).

https://doi.org/10.1016/j.actamat.2023.118728
Received 22 August 2022; Received in revised form 20 December 2022; Accepted 23 January 2023
Available online 25 January 2023
1359-6454/© 2023 Acta Materialia Inc. Published by Elsevier Ltd. All rights reserved.

stable state occurs spontaneously at intermediate temperatures, arising from the intrinsic metastability of the single-phase structure. Secondary BCC and close-packed-hexagonal (HCP) phases usually precipitate along grain boundary when subjected to annealing at a temperature below ~1000 °C [8–10]. For example, Senkov et al. [8] reported that a secondary Nb-Ta-rich BCC phase precipitates in the TiZrHfNbTa alloy even after a short period of annealing time (2 h). Chen et al. [9] found that the BCC matrix of TiZrHfNbTa RHEA decomposes into two phases, secondary Nb-Ta-rich BCC phase and Zr-Hf-rich HCP precipitates when annealing at 700 °C after 2.5 h. Additionally, the non-equimolar $Ti_{1.5}ZrHf_{0.5}Nb_{0.5}Ta_{0.5}$ RHEA equally cannot retain the BCC single-phase structure at intermediate temperatures [10]. As a promising alternative to conventional superalloys, retaining an invariable phase structure at working temperatures is essential. Otherwise, such phase decomposition undoubtedly leads to an increased risk of brittleness in thermally harsh environments. Our first primary motivation was to tune the composition of the TiZrHfNbTa RHEAs and enhance their phase stability at intermediate temperatures.

Besides the phase stability, another critical issue for the RHEAs that hinders their industrial applications is inadequate mechanical properties at room temperature, particularly for ductility compared to conventional superalloys. The well-known strength-ductility trade-off indicates that most strengthening mechanisms for increasing strength lead to ductility loss [11]. Several attempts have been made to improve the ductility of RHEAs by introducing heterogeneities to alter the planar slip mode of dislocations. For example, Lei et al. [12] proposed that adding a nonmetallic element, oxygen, could trigger a double cross-slip event in $(TiZrHfNb)_{98}O_2$ RHEAs. Specifically, the oxygen atoms preferentially interacted with Ti and Zr and tended to form (Ti, Zr, O)-based chemical short-range orderings (CSROs). Using a transmission electron microscope (TEM), the authors found a strong interaction between dislocations and CSROs. The CSROs divert moving dislocations and facilitate wavy slip of dislocations, resulting in enhanced dislocation multiplication. Therefore, the ductility of $(TiZrHfNb)_{98}O_2$ RHEA is much improved than the base TiZrHfNb RHEA in which the planar slip is the dominant mode [12]. Furthermore, An et al. [13] designed a ductile TiHfVNb RHEA using the constituent elements with a miscibility gap. The abundant nanometer-sized precipitation phase (β*) undergoes spinodal decomposition from the parent BCC phase (β). These periodically spaced β* makes dislocation motion sluggish and facilitates cross-slip routes as an alternative to planar slip. Owing to various slip modes, the spinodal-modulated TiHfVNb RHEA exhibits a large tensile elongation of 28% [13].

Although the research regarding ductility at room temperatures has achieved progress, a significant bottleneck is how to obtain these heterogeneous microstructures controllably. Considering that the aforementioned two successful cases [12,13] were both prepared by direct casting without any thermomechanical treatment, the need to involve the addition of oxygen [12] and spinodal decomposition [13], undoubtedly complicates the fabrication processes of RHEAs, particularly for large-scale casting ingots. Oxygen segregation is almost inevitable during solidification and might cause deleterious oxygen embrittlement if the local oxygen concentration is more than ~ 2 atomic percent (at.%) [12]. Also, the feasibility of obtaining the dispersive nanometer-sized β* in large-scale as-cast ingots of the TiHfNbV RHEA remains to be studied. It is naturally desirable to hunt for a new way to tailor microstructures without alloying elements that can give rise to deleterious embrittlement or uncontrollable precipitation behavior. Our second primary motivation was to improve the mechanical properties of RHEAs through a controllable thermomechanical treatment.

The present study employed the calculation of phase diagrams (CALPHAD) approach to optimize the alloy composition of the TiZrHfNbTa RHEAs and tune their phase stability. It was found that Ta and Hf were detrimental to the phase stability at intermediate temperatures. Therefore, the phase stability could be enhanced by (a) removing Ta and (b) replacing Hf with Ti and Zr from the same group of IVB on the periodic table. Accordingly, we designed and developed a Hf-depleted RHEA with the composition of $Ti_{30}Zr_{30}Hf_{16}Nb_{24}$ (at.%) (referred to as TZ30 hereafter), which showed outstanding thermostability. More importantly, numerous nanometer-sized precipitates were homogeneously formed in the TZ30 alloy after the thermomechanical treatment, leading to superior strength and ductility. The Ta-free and Hf-depleted TZ30 alloy also exhibited a lower material cost and density than the equimolar TiZrHfNbTa RHEA. This finding provided a paradigm for achieving superior thermostability and controllable precipitation behavior, which helped promote the industrial application of RHEAs.

2. Methods

Equilibrium phase diagrams were drawn, using Pandat software (version 2021) and PanHEAs thermodynamic database [14]. The TZ30 RHEA was prepared by a Ti-gettered vacuum arc melting from high-purity raw elements (> 99.95 wt percent, wt.%) and solidified in a water-cooled copper crucible. The button ingot was remelted and flipped at least six times to ensure a homogeneous distribution of elements. As-cast (AC) ingots were cold-rolled to a 70% reduction in thickness, followed by a recrystallization annealing at 900 °C for 20 min and air cooling (referred to as CR+A alloy hereafter). The specimens for stability tests were sealed in a vacuum quartz tube and then annealed at 600 °C for 200 h, followed by water quenching and breaking of the quartz tube (referred to as CR+A+ST alloy hereafter). The dog-bone-shaped tensile specimens with a gage size of $10 \times 2 \times 1.5\ mm^3$ were tested with the electronic universal testing machine (Sun-s-UTM4000) using a non-contact video extensometer (NCM-2D). The initial strain rate of the tensile test was set as $0.001\ s^{-1}$. Before testing, the specimen surfaces were ground down to 2000-grit SiC papers.

The phase structure was identified using an x-ray diffractometer (XRD, Empyrean-PANalytical) with Cu-Kα radiation in the 2θ range of 20° – 90° at a scanning speed of $4°{\cdot}min^{-1}$. The microstructures at the grain-size scale were characterized by a scanning electron microscope (Zeiss-Supra55) equipped with an electron back-scattering diffraction probe (EBSD, Oxford). The EBSD specimens were prepared by mechanical polishing and subsequent ion-beam milling. The EBSD data were analyzed by the HKL Channel 5 software. Electron probe microanalysis (EPMA, JXA-8530F Plus) equipped with a wavelength dispersive spectrometer (WDS) was also employed to characterize microstructures. Depending on the demand, the microstructures at the submicron scale were characterized by a TEM (FEI Talos F200X) at 200 kV. The high-resolution microstructures were characterized by an aberration-corrected TEM (FEI Titan G2) at 200 kV. The TEM specimens were prepared by mechanically grinding to 30 μm thickness and then ion milled with a Gatan 695. The TEM foil of the CR+A+ST sample was prepared by a focused ion beam (FIB, Helios G4 UX).

3. Results

3.1. Calculation of phase diagrams

Fig. 1 presents equilibrium phase diagrams of $M_x(TiZrHfNb)_{100-x}$ RHEAs, where M is a common refractory element from Groups IVB, VB, and VIB of the periodic table, and x ranges from 0 to 50 at% (in a particular case, x ranges from 0 to 33.3 at.% for Ti, Zr, Hf, and Nb). Phase stability at intermediate temperatures of $M_x(TiZrHfNb)_{100-x}$ RHEAs is the primary focus here. Secondary BCC, HCP, and C15-type Laves phases were the most frequent precipitated phases in $M_x(TiZrHfNb)_{100-x}$ RHEAs [Fig. 1 (a–i)]. $Hf_3Nb_2V_5$ intermetallic compounds also precipitated in the $V_x(TiZrHfNb)_{100-x}$ RHEAs [Fig. 1(d)]. Although V, Nb, Ta, Cr, Mo, and W are all regarded as a stabilizer of the BCC structure [15], interestingly, only the addition of Ti, Hf, and Nb could enlarge the single-phase region within a certain componential range at intermediate temperatures. Note that a board miscibility gap of $Ta_x(TiZrHfNb)_{100-x}$ led to a phase decomposition into two BCC phases at

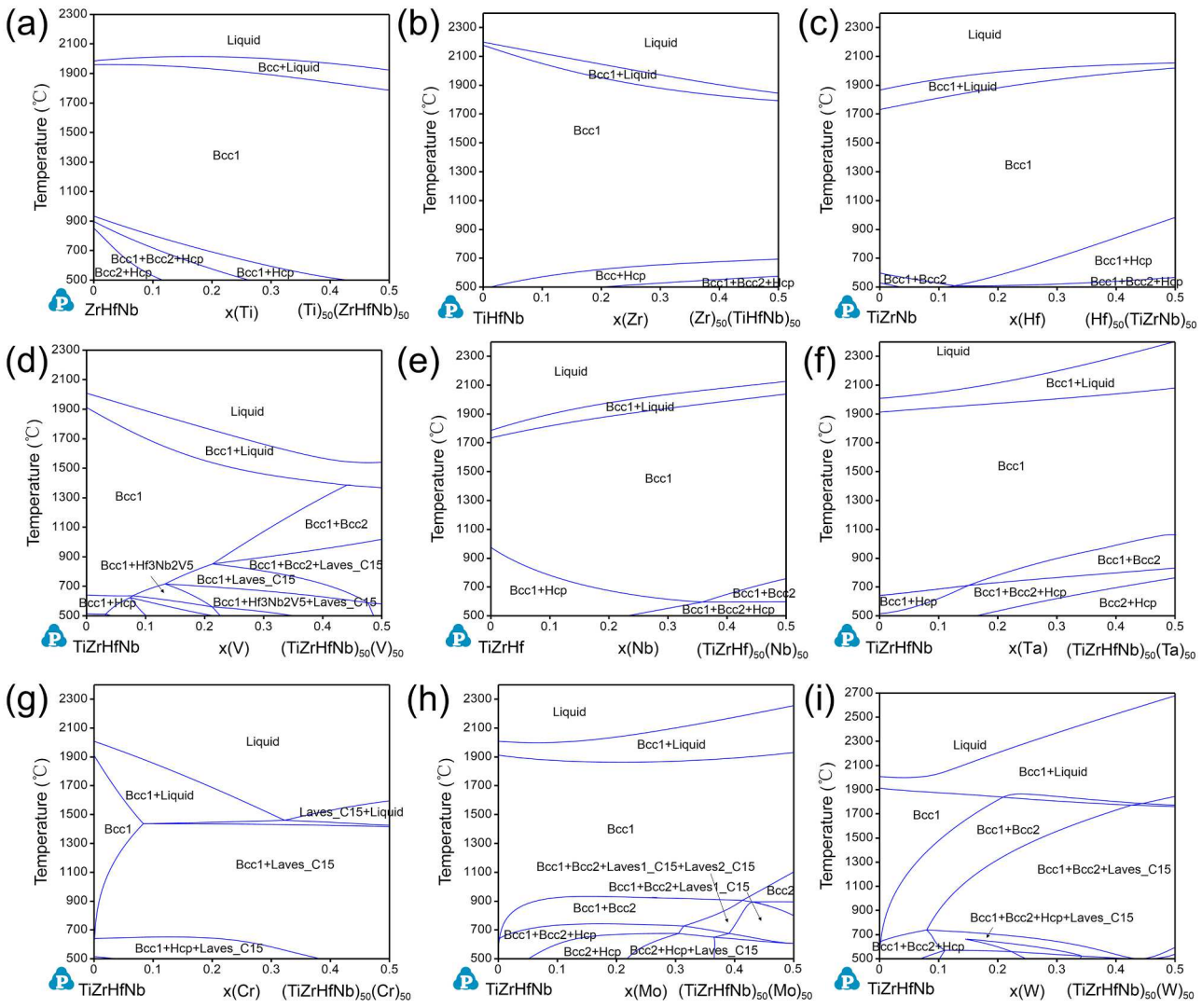

Fig. 1. Equilibrium phase diagrams of $M_x(TiZrHfNb)_{100-x}$ RHEAs. M is **(a)** Ti, **(b)** Zr, **(c)** Hf, **(d)** V, **(e)** Nb, **(f)** Ta, **(g)** Cr, **(h)** Mo, and **(i)** W.

intermediate temperatures [Fig. 1(f)]. Ta was detrimental to the phase stability of $M_x(TiZrHfNb)_{100-x}$ RHEAs regardless of concentration. Accordingly, Ta was removed to improve the phase stability of Ti-Zr-Hf-Nb-Ta RHEAs in the present work.

Besides the secondary BCC phase, the matrix BCC phase also transformed into the HCP phase and C15-type Laves phase. This indicates that the contribution from the mixing entropy in the Gibbs equation was no longer sufficient to suppress the mixing enthalpy at intermediate temperatures [e.g., $Cr_x(TiZrHfNb)_{100-x}$, as shown in Fig. 1(g)]. Although the addition of Zr would narrow the single-phase region, the overall single-phase region had the widest temperature range, where the lower bound of temperature for the single-phase region was just ~700 °C [Fig. 1(g)]. Therefore, Zr is useful for enhancing the thermal stability of $M_x(TiZrHfNb)_{100-x}$ RHEAs besides Ti, Hf, and Nb.

The above CALPHAD simulation indicates that the thermal stability of Ti-Zr-Hf-Nb RHEAs cannot be improved by adding alloying elements (except Ti, Zr, Hf, and Nb themselves), even though some of them are commonly regarded as BCC phase stabilizer. Optimizing the composition of Ti-Zr-Hf-Nb RHEAs is the best strategy to improve their thermal stability.

Accordingly, the composition of Ti-Zr-Hf-Nb RHEAs was optimized by plotting their isothermal sections of phase diagrams. Fig. 2(a–c) shows the pseudo-ternary phase diagram at 1200 °C, 900 °C, and 600 °C, respectively. Since Ti and Zr are in the same group of IVB with similar chemical properties on the periodic table, we regarded them as one category. As shown in Fig. 2(a), two broad BCC single-phase regions are nearby (Ti, Zr)-rich and Nb-rich corners at 1200 °C. With the increase in the Hf content, an HCP phase emerged near the Hf-rich corner. This feature indicated that Hf had a stronger tendency to form the HCP phase at 1200 °C than the other group of IVB elements, Ti and Zr. As the temperature dropped to 900 °C, a (Hf, Nb)-rich BCC phase, referred to as the BCC2 phase to distinguish it from the (Ti, Zr)-rich BCC1 phase, appeared in the (Ti, Zr)-depleted region [Fig. 2(b)]. Besides, a miscibility gap existed in the BCC1 and BCC2 regions near the Nb-rich corner. The BCC1 single-phase region at 900 °C became smaller than that at 1200 °C. As the temperature further dropped to 600 °C, a triple-phase coexistence of BCC1, BCC2, and HCP phases was observed in the central region of the phase diagram at 600 °C, indicating that the configurational entropy no longer dominated the phase selection at the intermediate temperature [Fig. 2(c)]. More importantly, the BCC1 single-phase region was further compressed into the (Ti, Zr)-rich corner. The equimolar TiZrHfNb RHEA, as marked by the triangle in Fig. 2(c), no longer remained a BCC structure at 600 °C.

Based on the CALPHAD results, a non-equimolar TZ30 RHEA located in the BCC1 single-phase region at 600 °C, as denoted by the pentagram in Fig. 2(c), was designed to reinforce the thermal stability of TiZrHfNb RHEAs at intermediate temperatures. Fig. 2(d) presents an equilibrium phase diagram in which the Nb content is fixed 24 at.%, obtained from

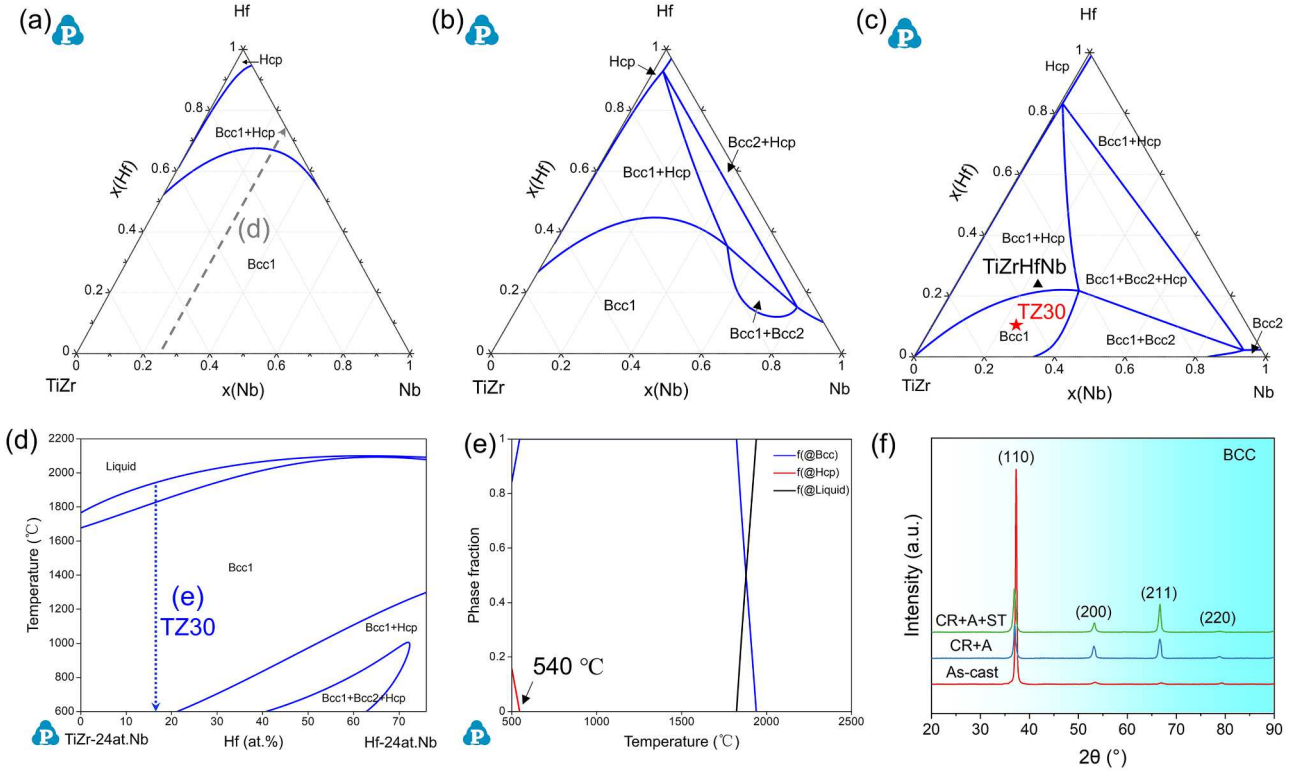

Fig. 2. Calculated phase diagrams of TiZrHfNb RHEAs. Isothermal-section phase diagram at **(a)** 1200 °C, **(b)** 900 °C, and **(c)** 600 °C. **(d)** Vertical-section phase diagram along the gray arrow in **(a)**, where the Nb content was fixed 24 at.%. **(e)** Equilibrium solidification phase diagram of the TZ30 alloy along the blue arrow in **(d)**. **(f)** XRD patterns of the as-cast, CR+A, and CR+A+ST TZ30 alloys.

the vertical section along the gray arrow in Fig. 2(a). As shown in Fig. 2(d), the BCC1 phase decomposes into the HCP and BCC2 phases in the temperature range from 600 to 1200 °C with the increasing Hf content, revealing that the excess Hf would weaken the stability of the BCC phase in Ti-Zr-Hf-Nb RHEAs. Fig. 2(e) shows the equilibrium solidification phase diagram of the TZ30 alloy along the arrow in Fig. 2(d). The BCC1 single-phase region could remain in a wide temperature range until the HCP phase precipitated at ~ 540 °C, showing satisfactory thermal stability.

A long-period thermal stability test, in which the TZ30 alloy was annealed at 600 °C for 200 h, was conducted to verify the accuracy of the aforementioned CALPHAD analysis. Fig. 2(f) shows the XRD patterns of the as-cast (AC) alloy, CR+A alloy, and CR+A plus thermal stability test (CR+A+ST) alloy. Only one set of BCC solid solutions diffraction peaks was detected from the XRD pattern [Fig. 2(f)] for three TZ30 alloys under different thermomechanical conditions, which agreed well with the corresponding CALPHAD results [Fig. 2(c–e)].

3.2. Initial microstructures

Fig. 3(a1) shows the back-scattered EPMA images of the AC TZ30 alloys. It is known that the contrast of back-scattered-electron imaging depends on atomic number (Z-contrast). Therefore, the bright-contrast dendritic region possessed a higher atomic number than the dark-contrast interdendritic region. This is because the elements with high melting points (i.e., Hf and Nb, which also have high atomic numbers) solidified earlier than those with low melting points (i.e., Ti and Zr). The corresponding WDS mapping [Fig. 3(a2)] shows that no obvious element segregation can be observed. To quantitatively measure the distribution of elements, WDS point scanning was performed for both dendritic and interdendritic regions. As shown in Table 1, the distribution of the element is relatively uniform even in the AC sample (only ~2% difference in atomic percent), indicating that the AC TZ30 alloy exhibited insignificant dendritic segregation.

Moreover, Fig. 3(b1, c1) displays the back-scattered EPMA images of CR+A and CR+A+ST alloys. Note that the dendritic trace was indistinct and almost invisible. This indicates that the microstructure of TZ30 alloy changed from dendrites (AC alloy) into equiaxed grains (CR+A and CR+A+ST alloys) after thermomechanical treatments. The WDS mapping [Fig. 3(b2, c2)] also confirmed a relatively uniform element distribution. Table 1 shows the WDS point scanning results, in which three scanning positions for each sample were chosen by random selection. There was slight composition fluctuation in the CR+A and CR+A+ST samples, and the actual composition was quite close to the nominal composition (~1% difference in atomic percent). Therefore, the possibility of a secondary BCC phase arising from element segregation can be excluded.

Fig. 3(a3, a4) provides an inverse pole figure (IPF) map and phase map of the AC TZ30 alloy, showing a columnar grain morphology where the growth direction of grains was parallel to the heat flux during solidification. The AC TZ30 alloy consisted of coarse grains with an average grain size of ~ 314 μm. In the CR+A and CR+A+ST conditions, both alloys consisted of equiaxed grains with almost random orientations [Fig. 3(b3, c3)]. After cold-rolling and recrystallization annealing, the mean grain size of CR+A alloy was effectively reduced to ~ 61 μm. On the other hand, the mean grain size of the CR+A+ST alloy was ~ 63 μm, indicating that the long-period annealing at 600 °C had not caused grain coarsening yet. The phase maps [Fig. 3(b4, c4)] revealed that the TZ30 alloys in the CR+A and CR+A+ST conditions were composed of the BCC phase with very little HCP phase after the thermomechanical treatment, which agrees well with the CALPHAD simulation [Fig. 2(e)] and XRD patterns [Fig. 2(f)].

Note that no coarse precipitated phase could be observed at grain boundaries for the CR+A+ST sample [Fig. 3(c1)]. Generally, nucleation and growth of the precipitated phase preferentially occur along grain boundaries because of heterogeneous nucleation and accelerated

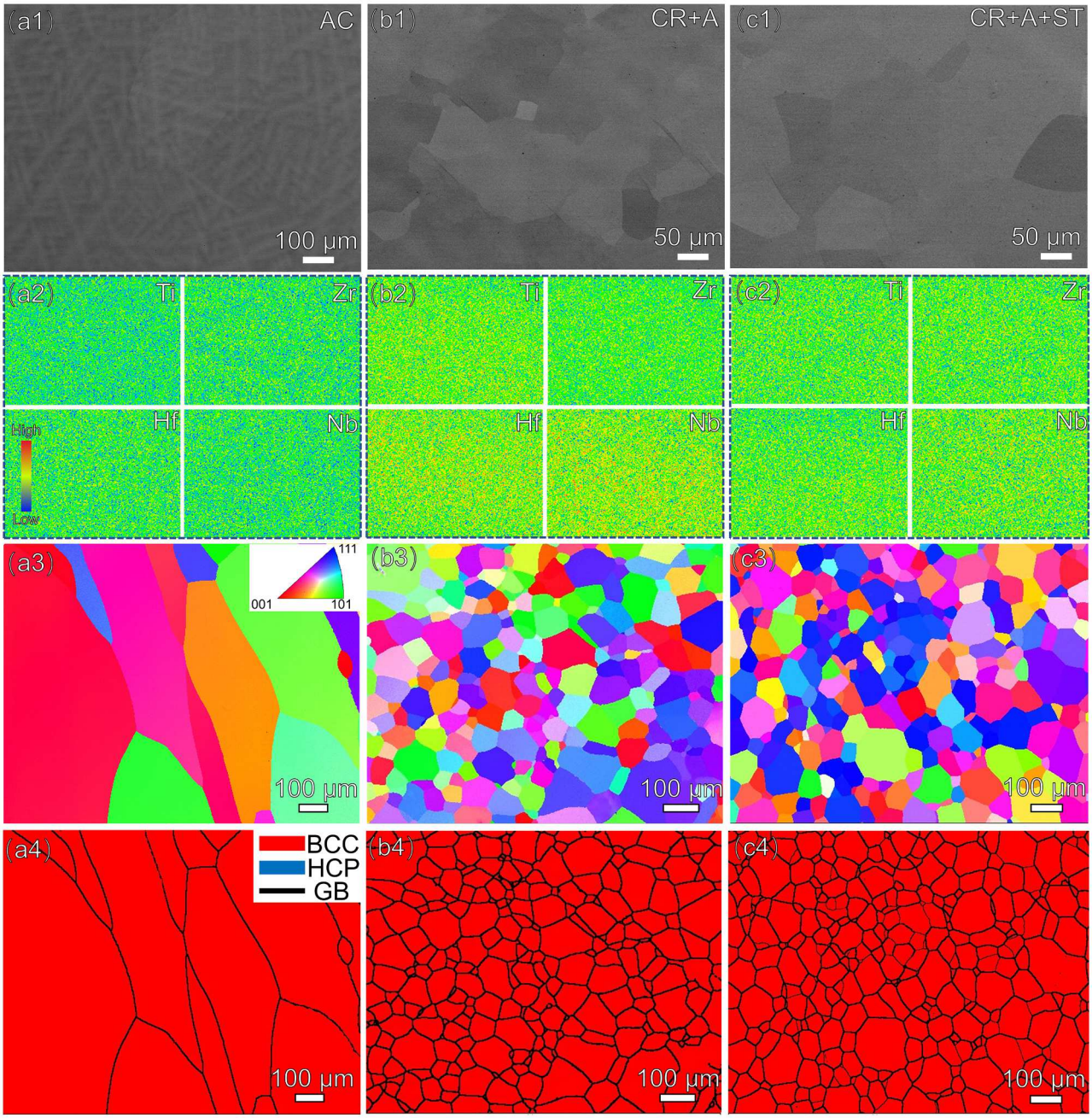

Fig. 3. Microstructures of the TZ30 alloy at the grain-size scale. Back-scattered EPMA images of **(a1)** AC, **(b1)** CR+A, and **(b3)** CR+A+ST alloy. WDS mapping of **(a2)** AC, **(b2)** CR+A, **(c2)** CR+A+ST alloy. EBSD IPF map of **(a3)** AC, **(b3)** CR+A, **(c3)** CR+A+ST alloy. EBSD phase map of **(a4)** AC, **(b4)** CR+A, **(c4)** CR+A+ST alloy.

Table 1
WDS point scanning results of the TZ30 alloy in the AC, CR+A, and CR+A+ST conditions.

Sample/Element content (at.%)		Ti	Zr	Hf	Nb
AC	dendritic region	30.4 ± 0.3	27.6 ± 0.3	17.5 ± 0.3	24.5 ± 0.3
	interdendritic region	32.0 ± 0.3	29.6 ± 0.4	16.3 ± 0.2	22.0 ± 0.3
CR+A		30.3 ± 0.3	29.9 ± 0.5	16.5 ± 0.3	23.3 ± 0.4
CR+A+ST		31.5 ± 0.7	29.0 ± 0.4	16.6 ± 0.4	22.8 ± 0.7

interfacial diffusion. For example, Chen et al. studied the phase transformations of TiZrHfNbTa high-entropy alloy annealing at 800 °C [9]. They found that precipitates with an irregular morphology were preferentially formed along grain boundaries after a short annealing time of 2.5 h [9]. Other examples include the phase transformations of TiZrHfTa [16] and $Al_xTiZrHfNb$ [17] alloys, in which precipitates are more likely to be observed at grain boundaries if phase decomposition occurs. In this sense, the TZ30 alloy designed by the CALPHAD approach had better thermal stability at intermediate temperatures than the above examples.

The aberration-correction scanning TEM (STEM) and selected-area electron diffraction (SAED) analyses were performed to further characterize the microstructure of the CR+A TZ30 alloy at the submicron scale. Fig. 4(a1) shows a high-angle annular dark-field (HADDF) image taken along the [001] zone axis of the BCC lattice. Note that numerous

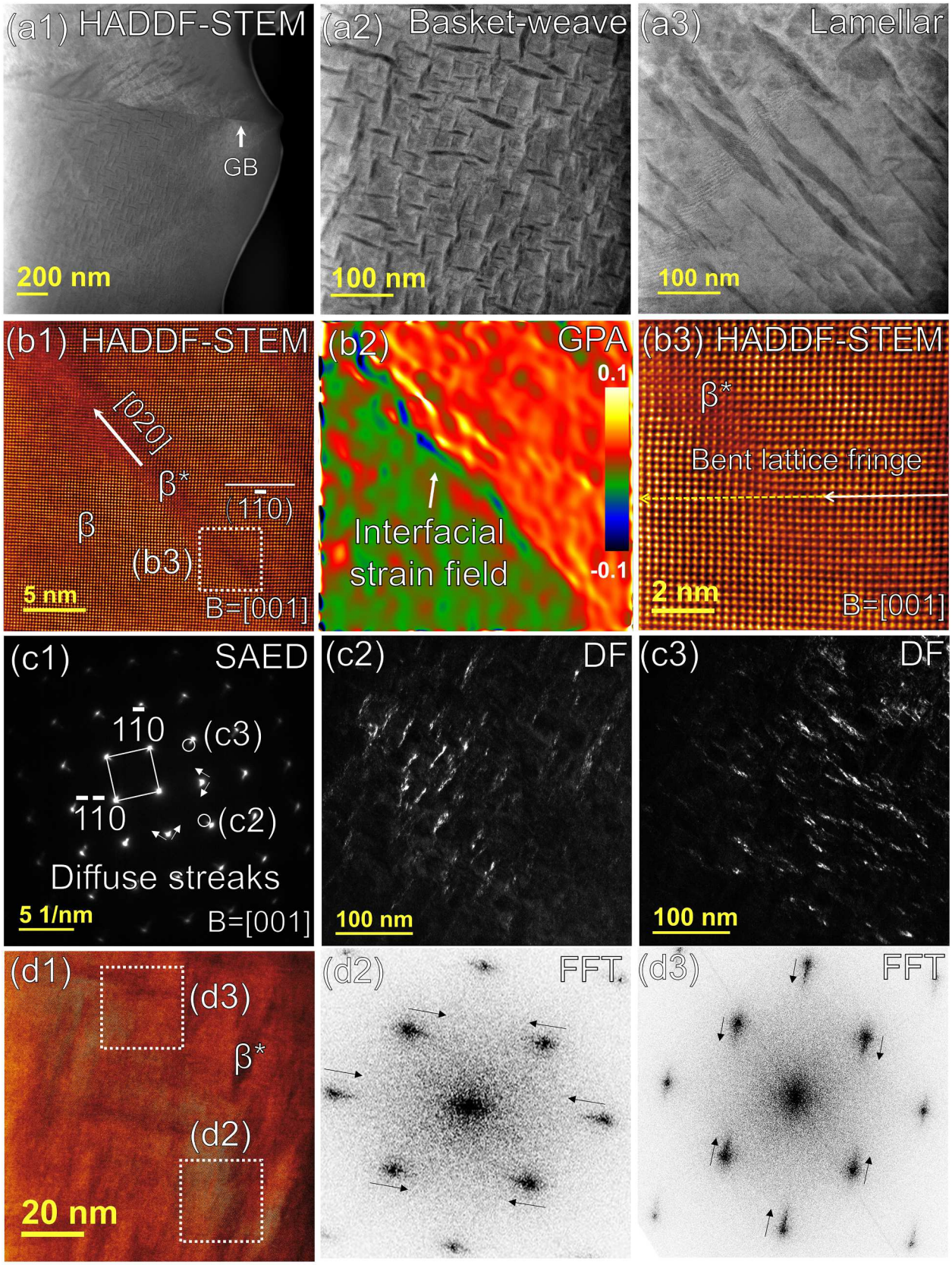

Fig. 4. TEM and SAED analyses of the CR+A TZ30 alloy. **(a1)** HADDF-STEM image; partially enlarged image in **(a2)** Basket-weave-like region and **(a3)** lamellar region. **(b1)** High-resolution HADDF-STEM image of the lamellar structure. **(b2)** GPA map, corresponding to **(b1). (b3)** Zoom-in image of the lamellar structure corresponding to the boxed region in **(b1). (c1)** SAED patterns from a basket-weave-like region. **(c2)** and **(c3)** Dark-field TEM micrographs taken in the diffraction condition of diffuse streaks corresponding to the circle in **(c1). (d1)** High-resolution HADDF-STEM image of the basket-weave-like structure. **(d2)** and **(d3)** FFTs obtained from the two boxed regions in **(d1).**

nanostructures were formed throughout the interior of grains. The zoom-in HADDF-STEM images revealed two kinds of morphologies for the nano-precipitates: basket-weave-like [Fig. 4(a2)] and lamellar structure [Fig. 4(a3)]. As shown in Table S1 (supplementary materials), the elemental distribution of the nano-precipitates with dark contrast was identified as a (Ti, Zr)-rich region through energy-dispersive spectroscopy (EDS). On the contrary, the bright-contrast matrix was a (Hf, Nb)-rich region. The basket-weave-like nano-precipitates had a width of ~ 10 nm and a length of ~ 80 nm [Fig. 4(a2)]. For lamellar nano-precipitates, the width ranged from 2 to 30 nm, and the length ranged from 30 to 300 nm [Fig. 4(a3)].

Fig. 4(b1) shows the high-resolution HADDF-STEM image of the interfacial regions between the matrix phase (β) and the lamellar nano-precipitates (β*), indicating that β* phase had an identical BCC lattice, and the boundary between the β and β* phase was a coherent interface. Fig. 4(b2) provides the lattice-strain maps obtained from the geometric phase analysis (GPA), corresponding to Fig. 4(b1). It was illustrated that a strong local strain field was distributed near the interfacial boundary. This strong strain field was triggered by bent lattice fringes, as depicted in Fig. 4(b3). The lattice fringes with $\langle 1\bar{1}0\rangle$ Miller indices bent from the β phase to the nano-sized β* phase. A slight deflection angle was seen between either side of the β phase, alongside the ⟨002⟩ growth direction of the lamellar β* phase [Fig. 4(b3)]. The growth direction of the β* phase depends on the lowest interfacial energy. The β* phase controlled by the spinodal decomposition mechanism possessed a fixed crystallographic orientation relationship with the matrix β phase, i.e., $(001)_{\beta} \parallel (001)_{\beta^*}$ and $[001]_{\beta} \parallel [001]_{\beta^*}$. Therefore, the β* phase tended to precipitate along the (001) habit plane of the β phase.

The bent lattice fringes, also referred to as local plane disorder [18], are also regarded to be the reasons for noticeable diffuse streaks exhibited in selected area electron diffraction (SAED) patterns [Fig. 4(c1)], where the Bragg spots stretched towards the shorter reciprocal vectors with ⟨200⟩ direction as indicated by the arrows in Fig. 4(c1). Dark-field TEM micrographs [Fig. 4(c2, c3)] taken in the diffraction condition of diffuse streaks revealed that the reflection of diffuse streaks belongs to the β* phase. Note that only one set of β* phase with the same growth direction was perpendicular to the corresponding reflection, as indicated by the circle in Fig. 4(c1). Fig. 4(d2, d3) respectively presents the fast Fourier transforms (FFTs) obtained from the two boxed regions in Fig. 4(d1). Different from symmetrical diffuse streaks in SAED pattern [Fig. 4(c1)], the asymmetric diffuse streaks obtained from FFTs direct towards only one principal axis. This is because only one set of a local β* phase perpendicular to a particular ⟨200⟩ direction was included. Similar diffuse streaks were also observed in some annealed RHEAs [18, 19] and Al-Cu alloys with Guinier-Preston (GP) zones [20]. The main reason for this phenomenon is the planar disorder between the matrix and the precipitated phase [21].

Interestingly, the β* phase observed in the CR+A condition was not present in the AC [Fig. S1 (supplementary materials)] and CR+A+ST conditions (Fig. 5). As illustrated in Fig. 5(a), the TEM foil was prepared from a grain boundary (GB) region in the CR+A+ST sample. Fig. 5(b, c) respectively shows the HADDF and BF TEM images, indicating that no secondary nano-precipitates could be found in the CR+A+ST alloy. Corresponding SAED [Fig. 5(d)] result also revealed that the CR+A+ST

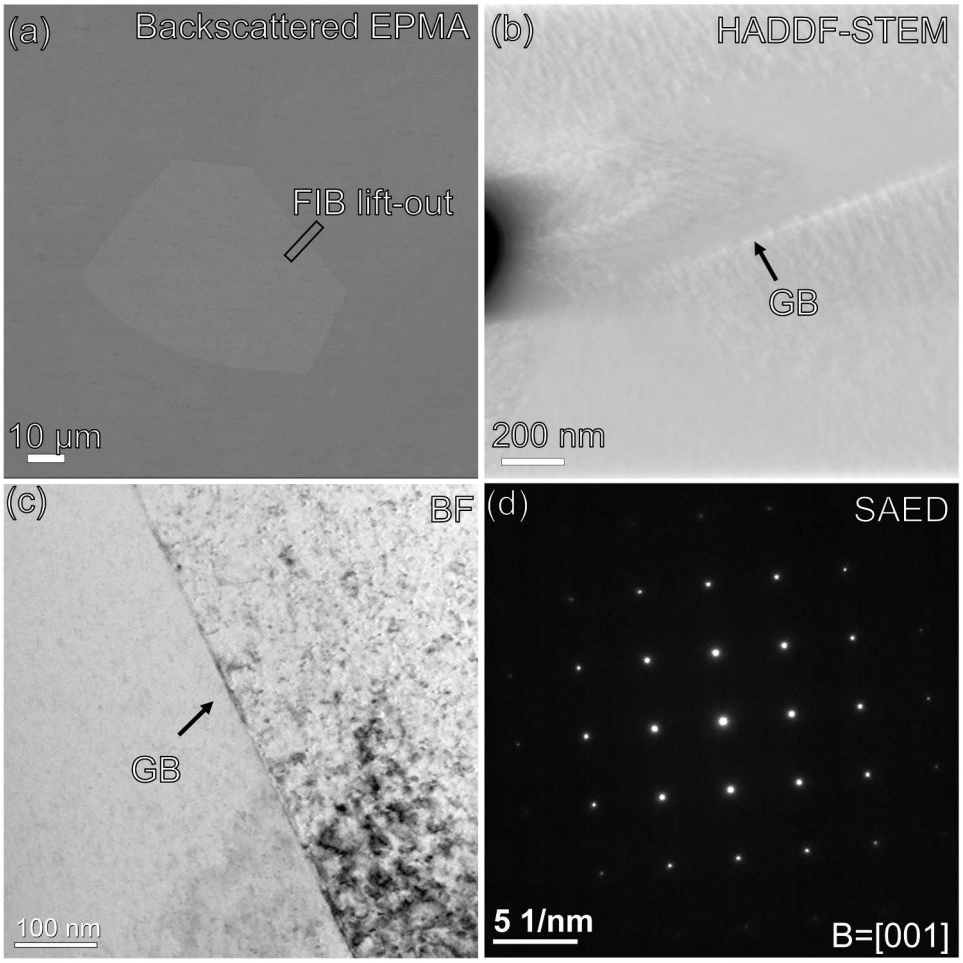

Fig. 5. High-resolution EMPA image and TEM analyses of the CR+A+ST TZ30 alloy. **(a)** EMPA image, showing a schematic diagram of the TEM foil prepared from the GB region. **(b)** HADDF-STEM and **(c)** BF image. **(d)** SAED patterns.

alloy exhibited a single BCC structure, different from the CR+A alloy with diffuse streaks [Fig. 4(c1)]. This trend implied that the nano-precipitates were formed during the cooling process. The formation mechanism of nano-precipitates will be discussed in Section 4.1.

3.3. Mechanical behavior

Fig. 6(a) provides the tensile engineering stress-strain curves of the TZ30 alloys in the AC, CR+A, and CR+A+ST conditions at room temperature. The yield strength ($\sigma_{0.2}$) and tensile ductility (ε) of the CR+A alloy were superior to those of the other two alloys. The average $\sigma_{0.2}$ increased from ~ 720 MPa for the AC alloy to ~ 800 MPa for the CR+A alloy. The unique feature in Fig. 6(a) was the outstanding fracture elongation of ~ 34.0% for the CR+A alloy, which increased by more than 54% compared with the AC alloy. In the CR+A+ST condition, annealing at 600 °C for 200 h resulted in a simultaneous decrease in $\sigma_{0.2}$ (730 MPa) and ε (25.6%), compared with the CR+A alloy. The corresponding true stress-strain curves [Fig. 6(b)] were obtained according to engineering stress-strain curves [Fig. 6(a)]. The work-hardening rate was calculated from the slope of true stress-strain curves. Over a wide range of strain (0 – 14%), the work-hardening rate for the CR+A and CR+A+ST alloys was sustained at a decent level, comparable to the flow stress. In other words, the strain distribution was at least relatively uniform. As the strain exceeded 14%, the work-hardening rate dropped rapidly and reduced to 0 MPa at the strain of ~ 16%, where inevitable necking occurred. For the AC alloy, the work-hardening rate was much less than the corresponding flow stress even in the early stage of strains, indicating that plastic instability and severe necking occurred at the beginning during tensile deformation. Fig. S2 presents the fractured surface of the TZ30 alloy in three conditions, showing ductile dimples without faceted cleavages.

Fig. 6(c) shows the comparison of mechanical properties of specific yield strength and fracture elongation between the CR+A TZ30 alloys and the previous representative RHEAs, for example, TiZrHfNbTa [5], TiZrHfNb [6], oxygen-doping TiZrHfNb [12], and transformation-induced plasticity $TiZrHfTa_x$ [22]. According to their processing history, all RHEAs were classified into two categories, AC (hollow dot) and CR+A (filled dot). As shown in Fig. 6(c), the TZ30 alloy possessed a comparatively low density (7.49 g/cm^3) due to the absence of heavy elements such as Ta, Mo, and W and the reduction in the use of heavy elements (i.e., Hf), giving rise to decent specific yield strength. Additionally, the CR+A TZ30 alloy exhibited excellent tensile ductility [Fig. 6(c)], almost better than that of the reported classical RHEAs [5,6,12,13,22-31].

The strain measurement by the digital image correlation (SMDIC) [32] was employed to map the full-field strain distribution during tensile deformation so as to uncover the mechanical behavior of the TZ30 alloy. Fig. 7(a) shows the strain field of the AC alloy within the gage length in different stages: the elastic stage, stable plastic stage, necking stage, and fracture stage. The strain localization appeared within the gage length even at the beginning and rapidly transformed into narrow bands. Fig. 7 (d) indicates that the local strain along the arrow, as marked in Fig. 7(a), was locally distributed into the middle of the gage length at a particular global strain. This implies that severe plastic instability or necking appeared earlier in the AC alloy [Fig. 7(a)] than that in the CR+A and CR+A+ST alloys, where the strain field is provided in Fig. 7(b, c).

The local strain of CR+A and CR+A+ST alloys was almost distributed uniformly throughout the entire loading area in the early deformation stage. Only a few strain localizations occurred within a narrow band at some locations. Subsequently, necking started to occur in the middle of the loading area in the necking stage, and obvious necking occurred in the fracture stage with a maximal local strain of 103.34% and 100.03% for the CR+A and CR+A+ST alloys, respectively. The local strain distribution of the CR+A and CR+A+ST alloys [Fig. 7(e, f)] was in line with the work-hardening curve, showing a relatively uniform strain distribution in a wide range of strains. No severe plastic instability was observed until the necking stage since the strain was distributed in a wide loading area [Fig. 7(b, c)].

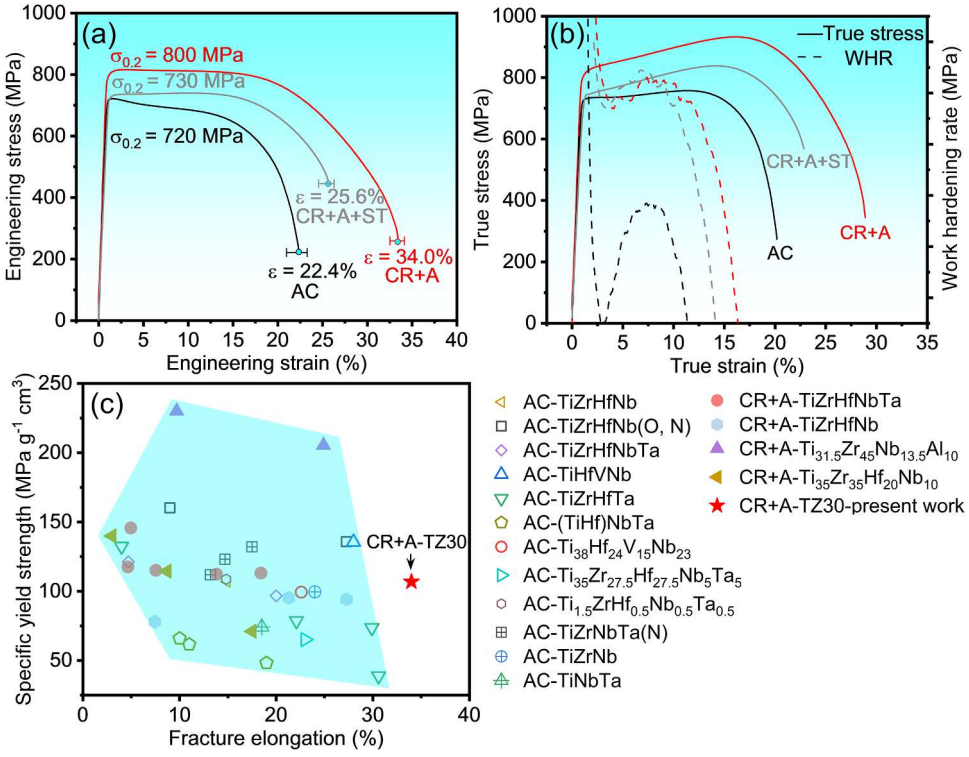

Fig. 6. Mechanical properties of the TZ30 alloy. **(a)** Engineering stress-strain curves. **(b)** True stress-strain curves and corresponding work-hardening rates of the AC, CR+A, and CR+A+ST alloys. **(c)** Comparing the CR+A TZ30 alloys and the previous representative RHEAs [5,6,12,13,22-31] regarding specific yield strength and fracture elongation.

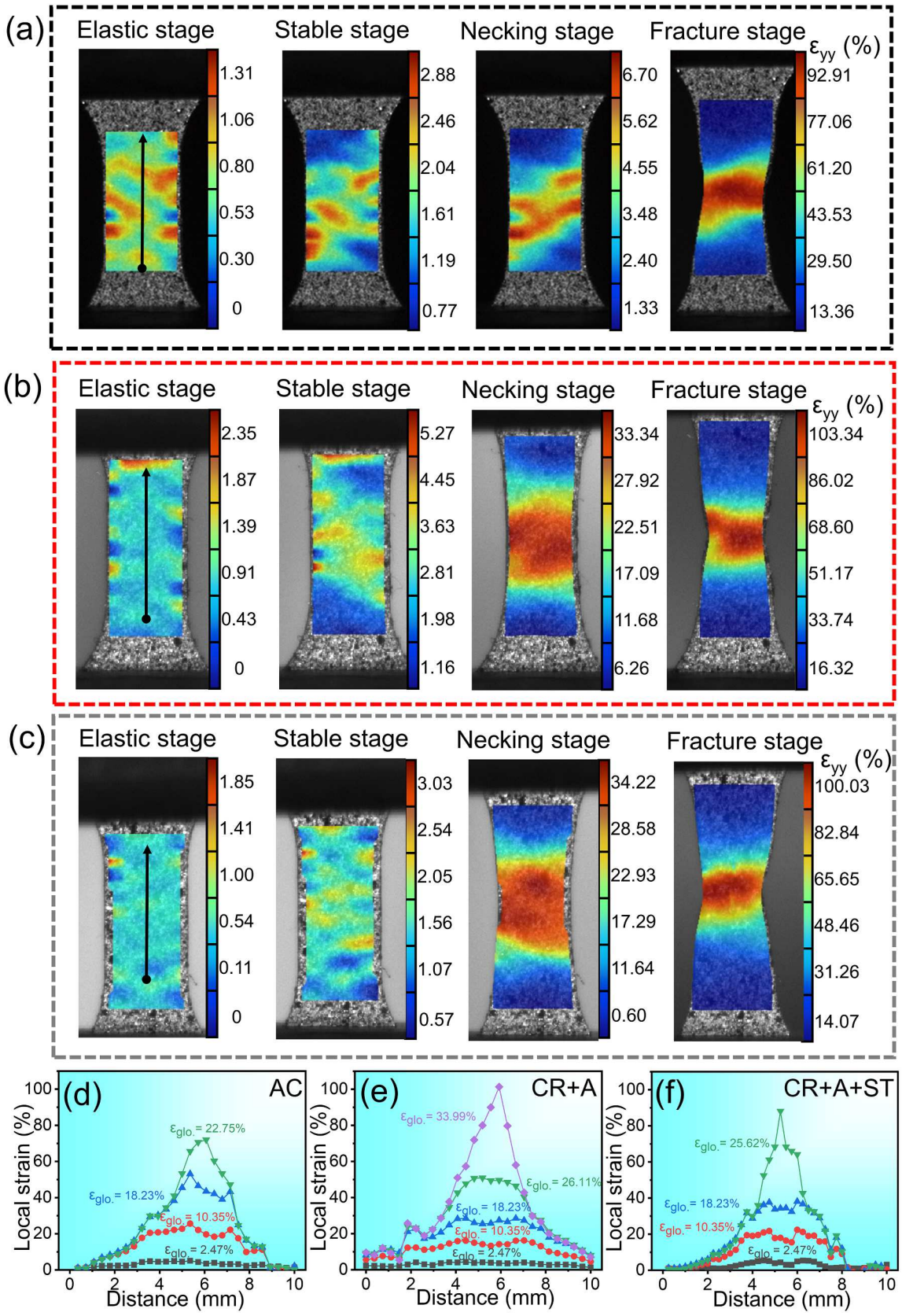

Fig. 7. Strain distributions obtained from the SMDIC of **(a)** AC, **(b)** CR+A, and **(c)** CR+A+ST alloy. Quantified local strain along the middle perpendicular direction of **(d)** AC, **(e)** CR+A, and **(f)** CR+A+ST alloy.

Despite possessing the same alloy composition, the mechanical behaviors of the three TZ30 alloys were entirely different, particularly in terms of the work-hardening capacity. Conducting a simple thermo-mechanical treatment not only broke the strength-ductility trade-off but also provided a more substantial work-hardening effect and resultant plastic stability. According to the previous investigation on the mechanical properties of RHEAs after cold-rolling and recrystallization annealing, the strengthening effect of grain refinement on strength is not obvious due to a severe lattice distortion and enhanced dynamic recovery in RHEAs [33]. Therefore, the improvement in mechanical properties could not simply be attributed to grain refinement. The strength contribution from different strengthening mechanisms will be discussed in Section 4.2.

3.4. Deformation microstructures

We first examined the deformation microstructures at the grain scale to unveil the origin of the unusual mechanical behavior of the CR+A alloy. Fig. 8(a, b) shows the EBSD IPF map of the CR+A alloy after fracture, which had a local strain of ~ 20% and ~ 100%, respectively. The crystal structures were still the BCC lattice, and no stress-induced phase transition occurred in the CR+A alloy during tensile deformation. Note that parallel band structures were formed in the CR+A alloy after deformation. As shown in Fig. 9(a, b), the crystal misorientation of the parallel bands was arbitrary but in the range of 25° – 30°, which eliminated the possibility of deformation twinning, which possesses a misorientation of 60° for (112) twinning and 50.5° for (332) twinning in BCC metals or alloys [34]. The features above indicated that the parallel bands were kink bands. Kink bands are considered the third type of deformation besides uniform dislocation slip and deformation twinning.

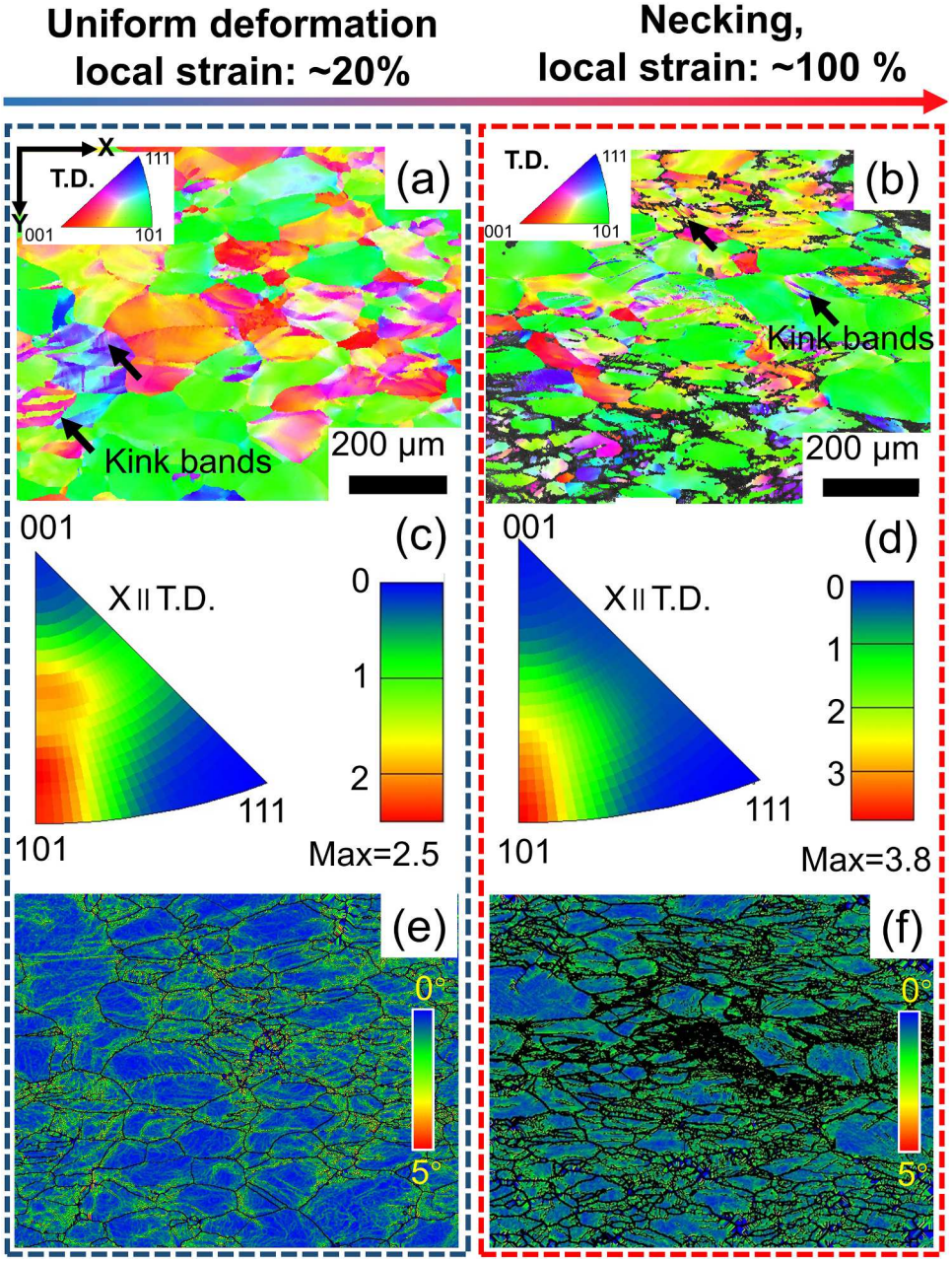

Fig. 8. EBSD IPF map of the CR+A alloy at **(a)** ~ 20% and **(b)** ~ 100% local strains. IPF at **(c)** ~ 20% and **(d)** ~ 100% local strain. KAM map at **(e)** ~ 20% and **(f)** ~ 100% local strains.

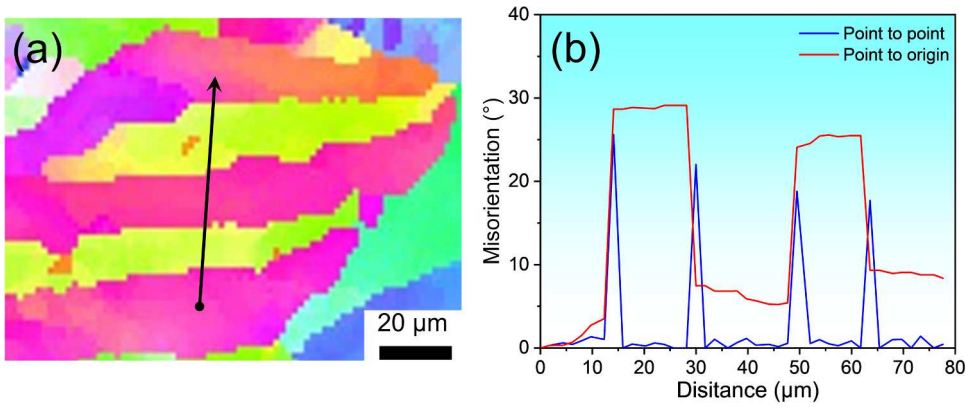

Fig. 9. **(a)** Microstructure of the kink band. **(b)** Local misorientation along the black arrow in **(a)**.

They are common in materials with high plastic anisotropy, such as HCP Zn alloys [35], but they are rare in BCC alloys with low plastic anisotropy. Only oxygen-containing β-Ti alloys [36] and some RHEAs with BCC lattices [34,37] tend to form kink bands. The kink bands have been frequently reported in TiZrHfNb(Ta) RHEAs under uniaxial tensile tests at various temperatures [38] and strain rates [39]. Meanwhile, the kink bands also appear during cold rolling [37] and fracture-toughness tests [40]. In this case, the formation of kink bands is considered to relieve stress concentration through the localized dislocation-mediated rotation and reduce the probability of fracture, improving the ductility without strength loss [37].

Besides the kink bands, the color of the IPF map is primarily green [Fig. 8(a, b)], indicating that the majority of ⟨101⟩ crystallographic orientations were parallel to the tensile direction. As shown in Fig. 8(c, d), the IPFs further confirmed the formation of a fiber texture with ⟨101⟩ crystallographic orientations, which is well-known as a typical tensile deformation texture in BCC metals and alloys [41]. As the local strain increased, the intensity of the ⟨101⟩ fiber texture was enhanced, manifested as an increase in the maximum intensity of texture from 2.5 to 3.8 [Fig. 8(c, d)]. Another feature in Fig. 8(a, b) was the color gradients

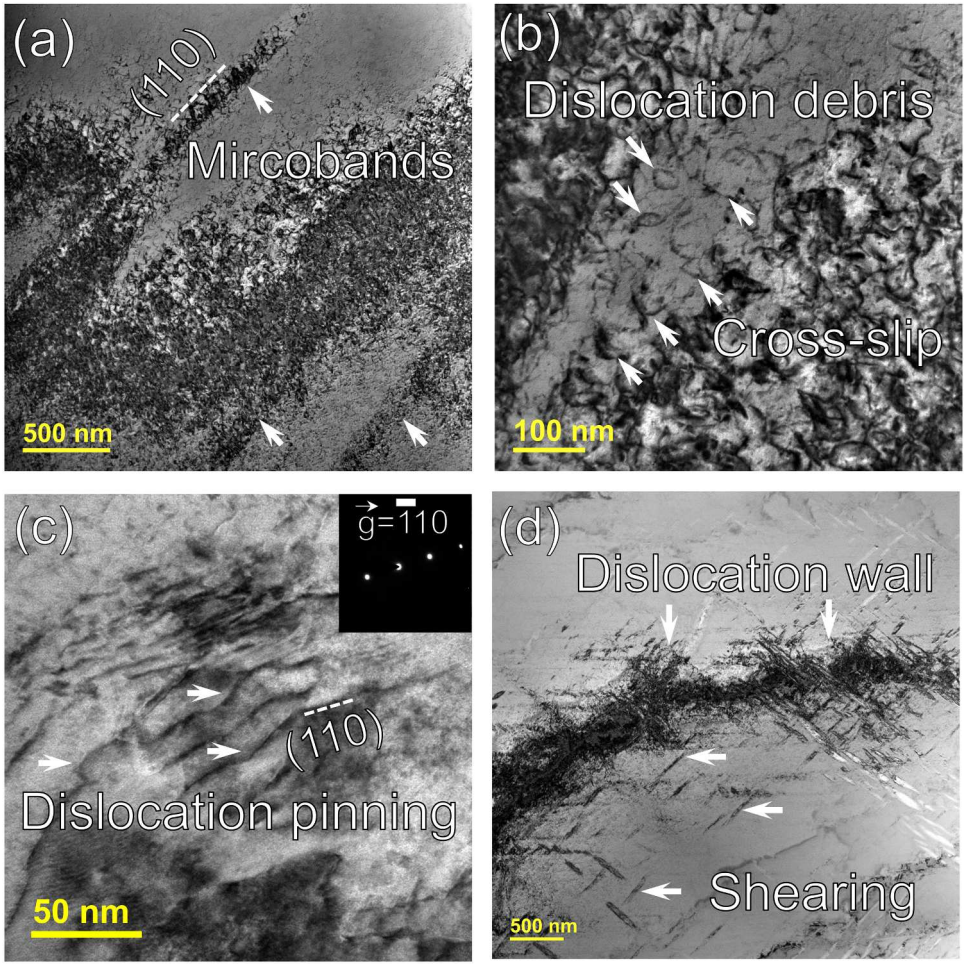

Fig. 10. Dislocation morphology of the CR+A TZ30 alloy obtained from a TEM under double-beam conditions: **(a)** microbands; **(b)** dislocation debris and cross-slip; **(c)** dislocation pinning; and **(d)** dislocation wall and dislocation shearing.

inside the deformed grains, which implied misorientations inside. Fig. 8 (e, f) present the kernel average misorientation (KAM) map, which depicted the density of geometrically necessary dislocations. The KAM value at the dislocation substructure and grain boundaries were higher than the intragranular ones, indicating that dislocations mainly accumulated at these places.

We further observed the deformation microstructure at the submicron scale through TEM under double-beam conditions. Fig. 10(a) presents the dislocation morphology of the CR+A alloy after fracture. Several microbands existed, which is one of the typical characteristics of planar slip. Once the leading dislocations crossed the barrier for gliding, successive dislocations could glide on the same plane, triggering a continuous coplanar slip [13]. Fig. 10(b) presents the zoom-in dislocation morphology, showing numerous short and curved dislocations. These curve features were signs of dislocation cross-slip, indicating that cross-slip was a supplementary slip mechanism besides planar slip. In addition to cross-slip, numerous loop-shaped dislocation debris, referred to as Orowan loops [42], are marked in Fig. 10(b). This dislocation debris is usually perceived as a cross-slip outcome [43]. As shown in Fig. 10(c), the straight screw dislocations were pinned and transformed into mixed dislocations. Different from the dislocation-pinning effect of interstitial atoms in carbon steels or oxygen-containing titanium alloys, the dislocations, in this case, were very likely to be pinned by the interfacial strain field between the nano-precipitates and matrix [Fig. 4 (b2)]. Meanwhile, one crucial intrinsic feature in HEAs, known as local chemical fluctuation, also acted as a roadblock for dislocation motion [44]. As the imposed plastic flow continuously increased, the second slip system was activated to accommodate the pinned dislocation. In other words, the cross-slip mechanism was activated to sustain the dislocation slip when encountering strong resistance. Fig. 10(d) shows the interaction between nano-precipitates and dislocations, revealing a dislocation-shearing mechanism rather than the Orowan bowing mechanism. The cross-slipped dislocations ultimately evolved into a dense dislocation wall, as marked in Fig. 10(d). The cross-slip in this case was clearly different from the previous equimolar TiZrHfNb alloy, in which the profuse long and straight screw dislocations tended to dominate [45]. The cross-slip played a vital role in the dislocation multiplication through Frank-Read sources, resulting in an enhanced work-hardening capacity and high tensile ductility [12].

4. Discussion

4.1. Formation mechanism of nano-precipitates

Abundant nano-precipitates appeared in the TZ30 alloy under the CR+A condition, but they were not present in the AC and CR+A+ST conditions. Therefore, the nano-precipitates were very likely to form during the cooling process. Fig. 11 depicts a schematic diagram of continuous cooling transformation (CCT) to reveal the formation mechanism of nano-precipitates. The CCT curves were drawn according to TEM results (Figs. 4,5, and S1) and CALPHAD simulation (Fig. 2). First of all, the equilibrium phase diagram of the TZ30 alloy [Fig. 2(e)] indicates that the temperature of phase transformation (from BCC to HCP) is 540 °C. If the temperature is closer to 540 °C, phase transformation's driving force (i.e., degree of supercooling) becomes smaller. As for transformation kinetics, the reverse applies. If the temperature is closer to 540 °C, transformation kinetics become faster. These two reasons lead to a C-shaped CCT curve.

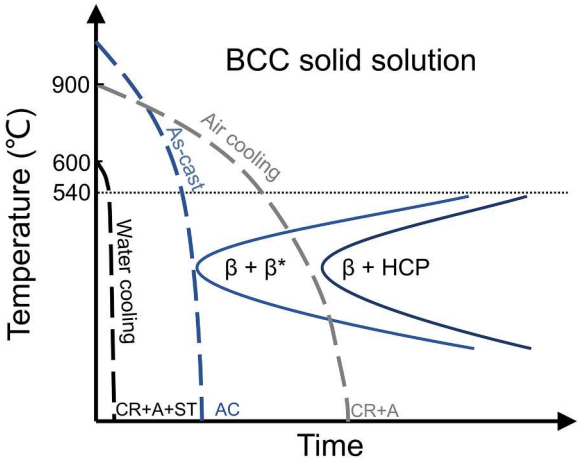

Fig. 11. Schematic diagram of CCT curves of the TZ30 alloy.

It should be noted that the cooling rate for the AC, CR+A, and CR+A+ST alloys was quite different. Specifically, the cooling rate of AC alloy solidified in a water-cooled copper crucible was much faster than the CR+A alloy, which was subjected to air cooling without a heat-transfer medium. Meanwhile, the CR+A+ST alloy that had undergone water cooling possessed the fastest cooling rate among the three conditions. Therefore, the AC, CR+A, and CR+A+ST alloys exhibited different phase transformation behaviors. Only the CR+A alloy with a relatively slow cooling rate satisfied the essential condition for nano-precipitates.

Moreover, spinodal decomposition, rather than the nucleation and growth mechanism, occurred in the CR+A alloy for the following reasons. First, Senkov et al. [46] pointed out the that the precipitation controlled by the nucleation and growth mechanism tends to result in multi-modal distributions consisting of micron-sized primary, submicron-sized secondary, and nanometer-sized tertiary precipitates. However, these multi-modal distributions of precipitates were not observed in the CR+A alloy. Second, nano-precipitates with lamellar and basket-weave morphology are representative modulated structures controlled by spinodal decomposition [13,18]. Actually, the essence of lamellar and basket-weave morphology is the same. Both are caused by uphill diffusion during spinodal decomposition, which produces periodic compositional wave patterns. Third, the precipitation kinetic of spinodal decomposition is much faster than that of the nucleation and growth mechanism because the latter needs to overcome a nucleation barrier. A short cooling time for the nano-precipitates observed in the CR+A alloy means that only spinodal decomposition meets the precipitation conditions, according to our scenario (Fig. 11). For the reasons given above, spinodal decomposition is regarded as the primary cause of nano-precipitates. Ti and Zr diffuse toward the precipitated phase during the cooling process, and Nb and Hf diffuse toward the matrix phase. These (Ti, Zr)-rich nano-precipitates would ultimately evolve into (Ti, Zr)-rich HCP phase under a premise of thermodynamic equilibrium, according to the CALPHAD simulation [Fig. 2(e)]. Therefore, the BCC structure of (Ti, Zr)-rich nano-precipitates is a metastable phase, in which the continuous enrichment of (Ti, Zr) solute can be regarded as a precursor for the HCP phase. With long-time annealing at the temperature below 540 °C, the enrichment of (Ti, Zr) solute would reach the limit and leads to a transformation of metastable BCC nano-precipitates into an HCP structure.

On the other hand, the mixing enthalpy between every two constituent elements (ΔH^{mix}_{A-B}), an indicator of their bonding energy, was another reason for nano-precipitates. According to Miedema's model [47], ΔH^{mix}_{Ti-Nb} (+2 kJ/mol) and ΔH^{mix}_{Zr-Nb} (+4 kJ/mol) were both greater than zero, indicating that Ti and Zr tended to separate from Nb. Moreover, ΔH^{mix}_{Ti-Zr} (0 kJ/mol) and ΔH^{mix}_{Hf-Nb} (−1 kJ/mol) approached zero, which provided a considerable solid solubility between these element pairs. Therefore, the formation of (Ti, Zr)-rich nano-precipitates during cooling was due to different chemical affinities between each constituent elements. Such nano-precipitates caused by the positive mixing enthalpy was also reported in other HEAs, for example, TiZrNbTa [19] (ΔH^{mix}_{Zr-Ta} and ΔH^{mix}_{Zr-Nb}) and AlCoCrCuFeNi (ΔH^{mix}_{Cu-Fe}) [48].

Fig. 12 depicts a schematic diagram to explain the two different

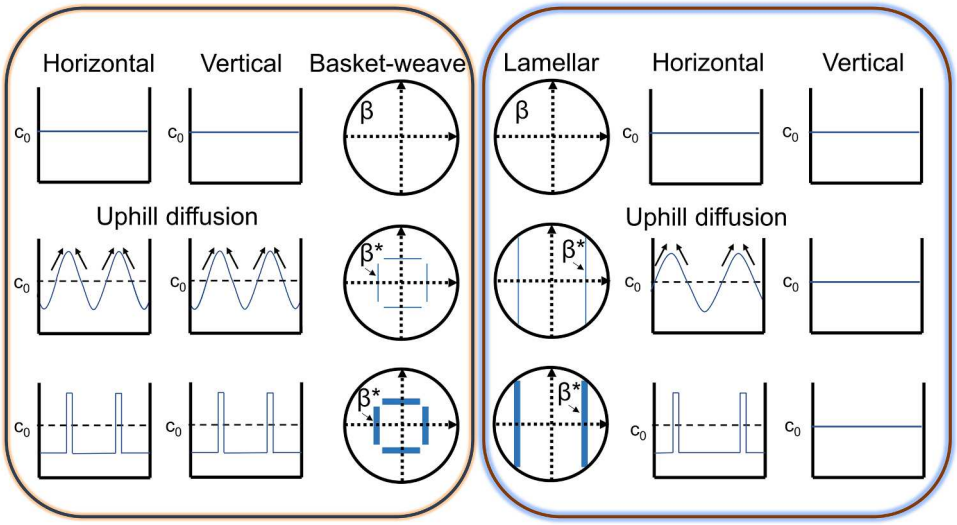

Fig. 12. Schematic diagram of the basket-weave and lamellar nanostructures.

morphologies of nano-precipitates [Fig. 4(a1)]. The circles in Fig. 12 indicate the morphology evolution during spinodal decomposition. The β* phase gradually precipitates from the parent β phase through an uphill diffusion mechanism. The difference between lamellar and basket-weave morphology is only one set of ⟨001⟩ growth orientation for the former but two sets for the latter. This different growth pattern might be connected with the initial mode of GP zones. The Y-axis of block diagrams depicts the composition of (Ti, Zr) solute along the arrows inside the corresponding circle. For the basket-weave structure, the composition of (Ti, Zr) solute fluctuates horizontally and vertically. However, the composition of (Ti, Zr) solute for lamellar structure fluctuates only in the horizontal direction but remains unchanged in the vertical direction. Since both structures process the same diffusion flux of solute, the basket-weave structure's wavelength is shorter than the lamellar structure.

4.2. Strengthening mechanism

The yield strengths of HEAs could be estimated using the following equation [49]:

$$\sigma_{YS} = \sigma_{YS}^{ROM} + \Delta\sigma_{SS} + \Delta\sigma_{GB} + \Delta\sigma_{PS} + \Delta\sigma_{DF} \tag{1}$$

where σ_{YS} is the yield strength, $\sigma_{YS}^{ROM} = \sum c_i\sigma_{YS}^i$ is the yield stress obtained by the rule of mixtures, and c_i and σ_{YS}^i are, respectively, the mole fraction and yield stress of the ith component in a solid solution. $\Delta\sigma$ represents the contribution from different strengthening mechanisms. Specifically, $\Delta\sigma_{SS}$ is the solution strengthening, $\Delta\sigma_{GB}$ is the grain-boundary strengthening, $\Delta\sigma_{PS}$ is the precipitate strengthening, and $\Delta\sigma_{DF}$ is the dislocation-forest hardening. In this case, the AC alloy, as well as the CR+A and CR+A+ST alloys that underwent sufficient annealing, were regarded to possess low dislocation density. Therefore, the $\Delta\sigma_{DF}$ was out of consideration here.

To begin with, a distorted elastic field due to the appearance of solute atoms acts as an obstacle to dislocation motion according to the classical solid-solution-strengthening theory. Senkov et al. developed a Labusch-type model applicable to the RHEA system according to the following equations [5,50]:

$$\Delta\sigma_{ssi} = fGc_i^{\frac{4}{3}}\delta_i^{\frac{2}{3}} \tag{2}$$

where $\Delta\sigma_{ssi}$ is the contribution of solid-solution strengthening from the ith component, f is a dimensionless constant with the value of 0.04, G is the shear modulus, and δ_i is the contribution of an elastic misfit from the ith component. δ_i is composed of the shear-modulus misfit (δ_G) and atomic-size misfit (δ_r), which can be described as [50]:

$$\delta_i = \sqrt{\delta_{Gi}^2 + \beta\delta_{ri}^2} \tag{3}$$

where β denotes a dimensionless constant in terms of dislocation categories. For a system containing a random mixture of edge and screw dislocations, β is designated as 9. δ_{ri} and δ_{Gi} can be calculated, employing the following equations [50]:

$$\delta_{ri} = \frac{9}{8}\sum c_j\delta_{rij} \tag{4}$$

$$\delta_{Gi} = \frac{9}{8}\sum c_j\delta_{Gij} \tag{5}$$

where δ_{Gij} and δ_{rij} are, respectively, the misfits of shear moduli and atomic sizes between the ith and jth components, which can be expressed as [50]:

$$\delta_{Gij} = 2\frac{G_i - G_j}{G_i + G_j} \tag{6}$$

$$\delta_{rij} = 2\frac{r_i - r_j}{r_i + r_j} \tag{7}$$

where G_i and r_i are the shear modulus and atomic size of the ith component, respectively. Then, $\Delta\sigma_{ss}$ can be calculated as [50]:

$$\Delta\sigma_{ss} = \left(\sum \Delta\sigma_{ssi}^{3/2}\right)^{2/3} \tag{8}$$

The yield strength, σ_{YS}, atomic radius, r, and shear modulus, G, of pure elements were obtained from the study by Senkov et al. [5], as shown in Table 2. According to Eq. (1 – 8), the calculated results of δ_{rij} and δ_{Gij} are given in Table 3. Accordingly, the calculated σ_{YS}^{ROM} and $\Delta\sigma_{SS}$ for the TZ30 alloy were 238.5 MPa and 481.4 MPa, respectively. The sum of σ_{YS}^{ROM} and $\Delta\sigma_{SS}$ was 719.9 MPa, which was very close to the

Table 2
Yield strength, σ_{YS}, atomic radius, r, and shear modulus, G, of pure elements at room temperature, obtained from Senkov et al. [5].

Element/Property	Ti	Zr	Hf	Nb	Ta
σ_{YS} (MPa)	195	280	240	240	170
r (nm)	0.1430	0.1551	0.1541	0.1429	0.1430
G (GPa)	44	33	30	38	69

Table 3
Calculated $\boldsymbol{\delta_{ri}}$ (bold numbers) and δ_{Gij} of the alloying element pairs.

Element i/j, $\boldsymbol{\delta_{ri}}$ /δ_{Gij}	Ti	Zr	Hf	Nb
Ti	0	**0.081**	**0.075**	**0.001**
Zr	0.286	0	**0.006**	**0.082**
Hf	0.378	0.095	0	**0.075**
Nb	0.146	0.141	0.235	0

measured yield strength of the as-cast alloy (720 MPa). This result accorded with the previous findings in terms of strengthening mechanism, in which $\Delta\sigma_{SS}$ played a critical role in the as-cast RHEAs with a single-phase BCC structure due to severe lattice distortion and comparatively low work-hardening capacity [49].

A radar map (Fig. 13) was illustrated to compare the normalized δ_{ri} and δ_{Gi} of the present TZ30 alloy and two equimolar model RHEAs, TiZrHfNb and TiZrHfNbTa alloy. δ_{rZr} had the highest values in all three alloys [Fig. 13(a)], indicating that Zr contributed the most to the atomic-size misfit due to the largest atomic radius of Zr atoms, compared with the other elements (Table 3). However, the difference in the atomic-size misfit among Ti, Zr, Hf, and Nb was inconspicuous, leading to a similar δ_{ri} for the TZ30 and TiZrHfNb alloys. On the contrary, Ti and Hf possessed the highest δ_{Gi} values in the TZ30 and TiZrHfNb alloys due to a distinct deviation from the average shear modulus, while the effect of Nb and Zr on δ_{Gi} was relatively insignificant. The aforementioned results revealed that substituting Hf with the mixture of Ti and Zr had little impact on the theoretical strength (719.9 MPa for the TZ30 alloy and 707.5 MPa for the TiZrHfNb alloy) because the TZ30 and TiZrHfNb alloys possessed nearly-equal δ_{Gi} and δ_{ri}. As for the TiZrHfNbTa alloy, the high shear modulus (69 GPa) of Ta, which was nearly twice as much as those of the other four elements, triggered a large δ_{Gi} and resultant high theoretical strength (906.4 MPa).

The contribution of grain-boundary strengthening ($\Delta\sigma_{GB}$) could be described by the classical Hall-Petch equation in which the relationship between the σ_{YS} and grain size was given as [51]:

$$\sigma_{YS} = \sigma_0 + \frac{K_{HP}}{\sqrt{D}} \tag{9}$$

where σ_0 is a constant that can be regarded as a lattice-friction stress, K_{HP} is a constant that can be considered as the grain-boundary resistance to slip transfer, and D is the average grain size that can be obtained from Fig. 3. Therefore, $\Delta\sigma_{GB}$ can be calculated using the following equation:

$$\Delta\sigma_{GB} = K_{HP}\left(\frac{1}{\sqrt{D_1}} - \frac{1}{\sqrt{D_2}}\right) \tag{10}$$

We applied Eq. (10) to calculate the strength contribution from the boundary strengthening. Substituting the D value and assigning K_{HP} of 240 MPa/μm$^{-1/2}$ from the study by Juan et al. [33], $\Delta\sigma_{GB}$ between the TZ30 alloys before and after thermomechanical treatment was about 17 MPa. This reselts is close to the measured σ_{YS} of AC and CR+A+ST alloys [Fig. 6(a)].

Moreover, the measured σ_{YS} difference between the CR+A and CR+A+ST was 70 MPa [Fig. 6(a)]. Due to the same chemical composition and similar grain size for the TZ30 alloys under the CR+A and CR+A+ST conditions, another strengthening mechanism, precipitate strengthening, $\Delta\sigma_{PS}$, contributed to the rest. We only adopted qualitative analysis on precipitation strengthening in this study owing to a relatively low value of $\Delta\sigma_{PS}$. Generally speaking, $\Delta\sigma_{PS}$ is attributed to both the classical Orowan-bypass and shearing mechanisms. In this case, however, no TEM evidence indicated that the Orowan-bypass mechanism occurred in the CR+A alloy. The shearing mechanism was considered to play a dominant role [Fig. 10(d)]. For the shearing mechanism, the strength increment originated from the shear modulus mismatch between the matrix and nano-precipitates, which could be described as [49]:

$$\Delta\sigma_{PS} = 0.0055D(\Delta G)^{\frac{2}{3}}\left(\frac{2f_p}{G_M}\right)^{\frac{1}{2}}\left(\frac{2r}{b}\right)^{\frac{3m-2}{2}} \tag{11}$$

where D is the Taylor factor, ΔG is the shear-modulus mismatch between the nano-precipitates and matrix, f_p is the volume fraction of the nano-precipitates, G_M is the shear modulus of the matrix, r is the average radius of the nano-precipitates, b is the Burgers vector, and m is a constant with a value of 0.85 [49]. Another possible explanation for the shearing mechanism was the interfacial strain field between the nano-precipitates and the matrix phase, which acted as an obstacle to dislocation motion [Fig. 4(b2)], leading to increased strength.

In summary, the $\Delta\sigma_{SS}$ contributed the most to the yield strength, while the grain refinement and nano-precipitates attributed more to ductility but played a minor role in yield strength. For the CR+A and CR+A+ST alloys, plastic deformation can be distributed homogeneously in a more significant number of grains, resulting in a smaller stress concentration and a better work-hardening capacity (Fig. 7). For the CR+A alloy, the dispersive nano-precipitates could locally pin the activated dislocations, facilitating an alternative cross-slip mechanism [Fig. 10(b)]. The resultant dislocation interaction promotes uniform plastic deformation and more considerable ductility.

Conclusions

The CALPHAD approach was employed to tailor the phase stability and mechanical properties of TiZrHfNb RHEAs. We successfully developed a novel Hf-depleted $Ti_{30}Zr_{30}Hf_{16}Nb_{24}$ (TZ30) RHEA with outstanding phase stability and superior mechanical properties. This

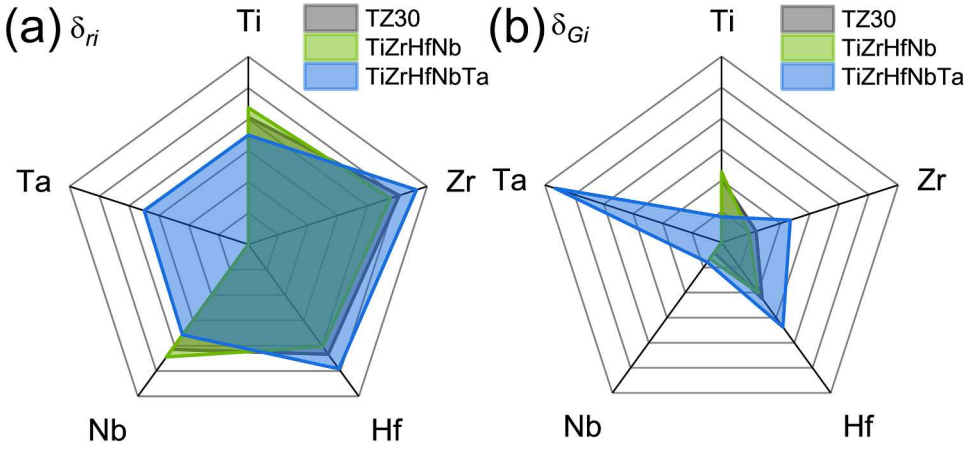

Fig. 13. Normalized δ_{ri} and δ_{Gi} from each element of the TZ30, TiZrHfNb, and TiZrHfNbTa alloys.

finding provided a paradigm for the superior thermostability and controllable nanophase-precipitation behavior in RHEAs. Some salient conclusions were drawn as follows:

(1) The phase diagrams of the $M_x(TiZrHfNb)_{100-x}$ quaternary system were drawn using the CALPHAD approach. Ta was detrimental to the phase stability of Ti-Zr-Hf-Nb-Ta RHEAs regardless of concentration. Moreover, Hf had a stronger tendency to form the HCP phase than Ti and Zr. As the temperature dropped to 600 °C, the single-phase region was compressed into the (Ti, Zr)-rich corner due to an appearance of the secondary BCC phase at the Nb-rich corner and the HCP phase at the Hf-rich corner. The Hf-depleted TZ30 alloy could remain as a single-phase BCC solid solution after annealing at 600 °C for 200 h, showing superior thermal stability.

(2) The as-cast TZ30 alloy consisted of coarse dendritic grains with an average grain size of ~ 314 μm. In the CR+A and CR+A+ST conditions, both alloys consisted of equiaxed grains with almost random orientations. The mean grain size of CR+A and CR+A+ST alloy was effectively reduced to ~ 61 and ~ 63 μm. On the other hand, numerous (Ti, Zr)-rich nano-precipitates dispersedly precipitated in the CR+A alloy. The nano-precipitates controlled by the spinodal decomposition mechanism had an identical BCC lattice and a coherent interface with the matrix phase. The lattice fringes with $(1\bar{1}0)$ Miller indices bent from the matrix phase to the nano-precipitates, causing a strong local strain field near the phase boundaries.

(3) The yield strength and tensile ductility of the CR+A alloy were both superior to those of the as-cast alloy. The CR+A alloy possessed a yield strength of ~ 800 MPa and a tensile fracture elongation of ~ 34.0%, showing a superior strength-ductility combination. The CR+A alloy also exhibited more substantial plastic stability than the as-cast alloy. The Labusch model uncovered that the solid-solution strengthening contributed the most to yield strength. Grain-boundary and precipitate strengthening played a minor role in yield strength.

(4) Kink bands were observed in the deformed CR+A alloy. The formation of the kink bands could relieve the stress concentration through the localized dislocation-mediated rotation and reduce the probability of fractures, improving the ductility of the CR+A alloy. Meanwhile, the dislocation cross-slip event occurred in the CR+A alloy, resulting in an enhanced dislocation multiplication through Frank-Read sources and a resultant work-hardening capacity.

Declaration of Competing Interest

The authors declare that they have no known competing financial interests or personal relationships that could have appeared to influence the work reported in this paper.

Acknowledgment

Supported by the National Key Research and Development Program of China (Nos. 2019YFA0209901 and 2018YFA0702901), the National Magnetic Confinement Fusion Energy Research and Development Program (No. 2018YFE0312400), National Natural Science Foundation of China (Nos. 51822402 and U20A20278), Liao Ning Revitalization Talents Program (No. XLYC1807047), and Major special project of "scientific and technological innovation 2025" in Ningbo (No. 2019B10086). PKL very much appreciates the supports from (1) the National Science Foundation (DMR – 1611180, 1809640, and 2226508) and (2) the US Army Research Office (W911NF-13–1-0438 and W911NF-19–2-0049).

Supplementary materials

Supplementary material associated with this article can be found, in the online version, at doi:10.1016/j.actamat.2023.118728.

References

[1] O.N. Senkov, D.B. Miracle, K.J. Chaput, J.P. Couzinie, Development and exploration of refractory high entropy alloys—a review, J. Mater. Res. 33 (19) (2018) 3092–3128.
[2] D.B. Miracle, M.H. Tsai, O.N. Senkov, V. Soni, R. Banerjee, Refractory high entropy superalloys (RSAs), Scr. Mater. 187 (2020) 445–452.
[3] D.B. Miracle, O.N. Senkov, A critical review of high entropy alloys and related concepts, Acta Mater. 122 (2017) 448–511.
[4] O.N. Senkov, D.B. Miracle, S.I. Rao, Correlations to improve room temperature ductility of refractory complex concentrated alloys, Mater. Sci. Eng. A 820 (2021), 141512.
[5] O.N. Senkov, J.M. Scott, S.V. Senkova, D.B. Miracle, C.F. Woodward, Microstructure and room temperature properties of a high-entropy TaNbHfZrTi alloy, J. Alloys Compd. 509 (20) (2011) 6043–6048.
[6] Y.D. Wu, Y.H. Cai, T. Wang, J.J. Si, J. Zhu, Y.D. Wang, X.D. Hui, A refractory Hf25Nb25Ti25Zr25 high-entropy alloy with excellent structural stability and tensile properties, Mater. Lett. 130 (2014) 277–280.
[7] B. Schuh, B. Völker, J. Todt, N. Schell, L. Perrière, J. Li, J.P. Couzinié, A. Hohenwarter, Thermodynamic instability of a nanocrystalline, single-phase TiZrNbHfTa alloy and its impact on the mechanical properties, Acta Mater. 142 (2018) 201–212.
[8] O.N. Senkov, S.L. Semiatin, Microstructure and properties of a refractory high-entropy alloy after cold working, J. Alloys Compd. 649 (2015) 1110–1123.
[9] S.Y. Chen, Y. Tong, K.K. Tseng, J.W. Yeh, J.D. Poplawsky, J.G. Wen, M.C. Gao, G. Kim, W. Chen, Y. Ren, R. Feng, W.D. Li, P.K. Liaw, Phase transformations of HfNbTaTiZr high-entropy alloy at intermediate temperatures, Scr. Mater. 158 (2019) 50–56.
[10] J.Q. Yao, X.W. Liu, N. Gao, Q.H. Jiang, N. Li, G. Liu, W.B. Zhang, Z.T. Fan, Phase stability of a ductile single-phase BCC Hf0.5Nb0.5Ta0.5Ti1.5Zr refractory high-entropy alloy, Intermetallics 98 (2018) 79–88.
[11] Z. Li, K.G. Pradeep, Y. Deng, D. Raabe, C.C. Tasan, Metastable high-entropy dual-phase alloys overcome the strength-ductility trade-off, Nature 534 (7606) (2016) 227–230.
[12] Z. Lei, X. Liu, Y. Wu, H. Wang, S. Jiang, S. Wang, X. Hui, Y. Wu, B. Gault, P. Kontis, D. Raabe, L. Gu, Q. Zhang, H. Chen, H. Wang, J. Liu, K. An, Q. Zeng, T.G. Nieh, Z. Lu, Enhanced strength and ductility in a high-entropy alloy via ordered oxygen complexes, Nature 563 (7732) (2018) 546–550.
[13] Z. An, S. Mao, T. Yang, C.T. Liu, B. Zhang, E. Ma, H. Zhou, Z. Zhang, L. Wang, X. Han, Spinodal-modulated solid solution delivers a strong and ductile refractory high-entropy alloy, Mater. Horizons 8 (3) (2021) 948–955.
[14] CompuTherm Software, Databases, in, https://computherm.com/panhea.
[15] P.J. Bania, Beta titanium alloys and their role in the titanium industry, JOM 46 (7) (1994) 16–19.
[16] H. Huang, Y. Sun, P. Cao, Y. Wu, X. Liu, S. Jiang, H. Wang, Z. Lu, On cooling rates dependence of microstructure and mechanical properties of refractory high-entropy alloys HfTaTiZr and HfNbTiZr, Scr. Mater. 211 (2022), 114506.
[17] Y. Wu, J. Si, D. Lin, T. Wang, W.Y. Wang, Y. Wang, Z. Liu, X. Hui, Phase stability and mechanical properties of AlHfNbTiZr high-entropy alloys, Mater. Sci. Eng. A 724 (2018) 249–259.
[18] S. Maiti, W. Steurer, Structural-disorder and its effect on mechanical properties in single-phase TaNbHfZr high-entropy alloy, Acta Mater. 106 (2016) 87–97.
[19] V.T. Nguyen, M. Qian, Z. Shi, X.Q. Tran, D.M. Fabijanic, J. Joseph, D.D. Qu, S. Matsumura, C. Zhang, F. Zhang, J. Zou, Cuboid-like nanostructure strengthened equiatomic Ti–Zr–Nb–Ta medium entropy alloy, Mater. Sci. Eng. A 798 (2020).
[20] T.J. Konno, K. Hiraga, M. Kawasaki, Guinier-Preston (GP) zone revisited: atomic level observation by HAADF-TEM technique, Scr. Mater. 44 (8) (2001) 2303–2307.
[21] A. Guinier, Heterogeneities in solid solutions, in: F. Seitz, D. Turnbull (Eds.), Solid State Physics, Academic Press, 1959, pp. 293–398.
[22] H. Huang, Y. Wu, J. He, H. Wang, X. Liu, K. An, W. Wu, Z. Lu, Phase-transformation ductilization of brittle high-entropy alloys via metastability engineering, Adv. Mater. 29 (30) (2017), 1701678.
[23] S.-P. Wang, E. Ma, J. Xu, New ternary equi-atomic refractory medium-entropy alloys with tensile ductility: hafnium versus titanium into NbTa-based solution, Intermetallics 107 (2019) 15–23.
[24] S. Wei, S.J. Kim, J. Kang, Y. Zhang, Y. Zhang, T. Furuhara, E.S. Park, C.C. Tasan, Natural-mixing guided design of refractory high-entropy alloys with as-cast tensile ductility, Nat. Mater. 19 (2020) 1175–1181.
[25] O.N. Senkov, A.L. Pilchak, S.L. Semiatin, Effect of cold deformation and annealing on the microstructure and tensile properties of a HfNbTaTiZr refractory high entropy alloy, Metall. Mater. Trans. A 49 (7) (2018) 2876–2892.
[26] R.R. Eleti, N. Stepanov, N. Yurchenko, S. Zherebtsov, F. Maresca, Cross-kink unpinning controls the medium- to high-temperature strength of body-centered cubic NbTiZr medium-entropy alloy, Scr. Mater. 209 (2022), 114367.
[27] J. Zýka, J. Málek, J. Veselý, F. Lukáč, J. Čížek, J. Kuriplach, O. Melikhova, Microstructure and room temperature mechanical properties of different 3 and 4 element medium entropy alloys from HfNbTaTiZr system, Entropy 21 (2019) 114.

[28] I.A. Su, K.-.K. Tseng, J.W. Yeh, B. El-Sayed, C.H. Liu, S.H. Wang, Strengthening mechanisms and microstructural evolution of ductile refractory medium-entropy alloy Hf20Nb10Ti35Zr35, Scr. Mater. 206 (2022), 114225.
[29] X. Yan, P.K. Liaw, Y. Zhang, Ultrastrong and ductile BCC high-entropy alloys with low-density via dislocation regulation and nanoprecipitates, J. Mater. Sci. Technol. 110 (2022) 109–116.
[30] S. Sheikh, S. Shafeie, Q. Hu, J. Ahlström, C. Persson, J. Veselý, J. Zýka, U. Klement, S. Guo, Alloy design for intrinsically ductile refractory high-entropy alloys, J. Appl. Phys. 120 (16) (2016), 164902.
[31] L. Lilensten, J.P. Couzinié, J. Bourgon, L. Perrière, G. Dirras, F. Prima, I. Guillot, Design and tensile properties of a bcc Ti-rich high-entropy alloy with transformation-induced plasticity, Mater. Res. Lett. 5 (2) (2017) 110–116.
[32] Y. Lu, X. Gao, L. Jiang, Z. Chen, T. Wang, J. Jie, H. Kang, Y. Zhang, S. Guo, H. Ruan, Y. Zhao, Z. Cao, T. Li, Directly cast bulk eutectic and near-eutectic high entropy alloys with balanced strength and ductility in a wide temperature range, Acta Mater. 124 (2017) 143–150.
[33] C.C. Juan, M.H. Tsai, C.W. Tsai, W.L. Hsu, C.-.M. Lin, S.K. Chen, S.-.J. Lin, J.-.W. Yeh, Simultaneously increasing the strength and ductility of a refractory high-entropy alloy via grain refining, Mater. Lett. 184 (2016) 200–203.
[34] M. Wu, S. Wang, F. Xiao, G. Zhu, C. Yang, D. Shu, B. Sun, Dislocation glide and mechanical twinning in a ductile VNbTi medium entropy alloy, J. Mater. Sci. Technol. 110 (2022) 210–215.
[35] E. Orowan, A type of plastic deformation new in metals, Nature 149 (3788) (1942) 643–644.
[36] Y. Yang, S.Q. Wu, G.P. Li, Y.L. Li, Y.F. Lu, K. Yang, P. Ge, Evolution of deformation mechanisms of Ti–22.4Nb–0.73Ta–2Zr–1.34O alloy during straining, Acta Mater 58 (7) (2010) 2778–2787.
[37] S. Wang, M. Wu, D. Shu, B. Sun, Kinking in a refractory TiZrHfNb0.7 medium-entropy alloy, Mater. Lett. 264 (2020), 127369.
[38] S. Wang, M. Wu, D. Shu, G. Zhu, D. Wang, B. Sun, Mechanical instability and tensile properties of TiZrHfNbTa high entropy alloy at cryogenic temperatures, Acta Mater 201 (2020) 517–527.
[39] G. Dirras, H. Couque, L. Lilensten, A. Heczel, D. Tingaud, J.P. Couzinié, L. Perrière, J. Gubicza, I. Guillot, Mechanical behavior and microstructure of Ti20Hf20Zr20Ta20Nb20 high-entropy alloy loaded under quasi-static and dynamic compression conditions, Mater. Charact. 111 (2016) 106–113.
[40] X.J. Fan, R.T. Qu, Z.F. Zhang, Remarkably high fracture toughness of HfNbTaTiZr refractory high-entropy alloy, J. Mater. Sci. Technol. 123 (2022) 70–77.
[41] B. Sander, D. Raabe, Texture inhomogeneity in a Ti-Nb-based beta-titanium alloy after warm rolling and recrystallization, Mater. Sci. Eng. A 479 (1–2) (2008) 236–247.
[42] J. Zhang, W.Z. Han, Oxygen solutes induced anomalous hardening, toughening and embrittlement in body-centered cubic vanadium, Acta Mater 196 (2020) 122–132.
[43] R. Wang, Y. Tang, Z. Lei, Y. Ai, Z. Tong, S. Li, Y. Ye, S. Bai, Achieving high strength and ductility in nitrogen-doped refractory high-entropy alloys, Mater. Des. (2022) 213.
[44] Q. Ding, Y. Zhang, X. Chen, X. Fu, D. Chen, S. Chen, L. Gu, F. Wei, H. Bei, Y. Gao, M. Wen, J. Li, Z. Zhang, T. Zhu, R.O. Ritchie, Q. Yu, Tuning element distribution, structure and properties by composition in high-entropy alloys, Nature 574 (7777) (2019) 223–227.
[45] J.P. Couzinie, L. Lilensten, Y. Champion, G. Dirras, L. Perriere, I. Guillot, On the room temperature deformation mechanisms of a TiZrHfNbTa refractory high-entropy alloy, Mater. Sci. Eng. A 645 (2015) 255–263.
[46] O.N. Senkov, D. Isheim, D.N. Seidman, A.L.J.E. Pilchak, Development of a refractory high entropy superalloy, Entropy 18 (3) (2016) 102.
[47] A. Takeuchi, A. Inoue, Classification of bulk metallic glasses by atomic size difference, heat of mixing and period of constituent elements and its application to characterization of the main alloying element, Mater. Trans. 12 (2005) 2817.
[48] S. Singh, N. Wanderka, B.S. Murty, U. Glatzel, J. Banhart, Decomposition in multi-component AlCoCrCuFeNi high-entropy alloy, Acta Mater. 59 (1) (2011) 182–190.
[49] S.M. Chen, Z.-.J. Ma, S. Qiu, L.J. Zhang, S.Z. Zhang, R. Yang, Q.M. Hu, Phase decomposition and strengthening in HfNbTaTiZr high entropy alloy from first-principles calculations, Acta Mater 225 (2022), 117582.
[50] H.W. Yao, J.W. Qiao, J.A. Hawk, H.F. Zhou, M.W. Chen, M.C. Gao, Mechanical properties of refractory high-entropy alloys: experiments and modeling, J. Alloys Compd. 696 (2017) 1139–1150.
[51] Z.C. Cordero, B.E. Knight, C.A. Schuh, Six decades of the Hall–Petch effect – a survey of grain-size strengthening studies on pure metals, Int. Mater. Rev. 61 (8) (2016) 495–512.